Exploring super-resolution for the downscaling of urban flood simulations

Katia Ait-Ameur, Vincent Guinot, Luis Martí, Antoine Rousseau, Gwladys Toulemonde

Exploring super-resolution for the downscaling of urban flood simulations

Katia Ait-Ameur,* Vincent Guinot,† Luis Marti,‡ Antoine Rousseau,*
Gwladys Toulemonde§

February 10, 2025

Abstract

Two-dimensional hydrodynamic models are computationally expensive. This drawback can limit their application to solving problems requiring real-time predictions or several simulation runs. To resolve fine-scale physical processes, allowing for local impact assessments, downscaling techniques are essential. Super-resolution is an innovative technique that upscales the resolution of an image and thus enables to reconstruct high-fidelity images from low-resolution data. This study performs super-resolution analysis for spatial downscaling of hydrodynamic data using various deep learning techniques to reconstruct high-resolution flow fields from low-resolution flow field data. It increases the spatial resolution of coarsened water depth and unit discharge norm from 4 m to 80 cm. The training data for these models was generated using a physically based hydrodynamic model. To evaluate their performance and accuracy, multiple tests were conducted using synthetic events. Our experiments indicate that these models successfully predicted water depths in the testing flood scenario for the dynamic case but could not preserve the steady states during the reconstruction. Furthermore, these models cannot satisfactorily generalize to flood scenario outside the training datasets with different boundary conditions. The results demonstrate that the proposed models are up to 30 times faster than the hydrodynamic model and promising in terms of accuracy. Therefore, it bridges the gap between detailed flood modelling and real-time applications.

Introduction

Fast and accurate flood prediction is a crucial factor in decision-making and operational strategies, especially when human lives are at stake. Climate change is likely to increase the frequency and intensity of extreme storm events, which can potentially magnify the impacts of flooding [7]. Flood modeling is a fundamental tool for planning and designing flood mitigation in urban areas. Two-dimensional (2D) hydrodynamic approaches such as shallow water models are the most effective models used for urban flood predictions [24]. However, they are computationally expensive, hampering their application in large-scale watersheds or when many runs are required. For this reason, upscaled shallow water models have been under development over the past two decades ([4, 14, 25, 12, 32, 13, 10, 29]). A salient advantage of upscaled shallow water models is their computational efficiency, with CPU times two to three orders of magnitude smaller than those of classical shallow water models ([12, 17, 13]). The price to pay for the computational efficiency of an upscaled model is the coarseness of the approach. The simulation results are provided in the form of upscaled (or averaged) flow variables over computational cells the size of one to several houses, typically 10 to 50 m. For practical purposes such as flood hazard mapping, however, the knowledge of the flow fields is required with a much finer resolution. Since hazard indicators are often strongly non-linear with respect to the flow

*Inria LEMON, Inria, Univ. Montpellier, France
†HydroSciences Montpellier (HSM), Univ. Montpellier, CNRS, IRD, Montpellier, France
‡Inria Chile Research Center, Santiago, Chile.
§IMAG, Univ. Montpellier, CNRS, Montpellier, France

variables, using only coarse scale averages cannot be expected to yield reliable assessments. Therefore, a form of downscaling of the upscaled model simulations is needed to perform relevant hazard assessment. The downscaling process has been little explored in comparison to the upscaling strategy, although interest for the approach has started to emerge from the recent literature [5, 3].

In the context of climate change studies, downscaling methods have been developed and applied to increase the resolution of climate model outputs. These methods include statistical and dynamical downscaling using regional climate models, as well as AI-based downscaling that leverages neural networks (NNs), which have become increasingly popular in recent years. The AI-based downscaling methods are based on the image super-resolution (SR) approach which originates from computer vision, see [1] for a review. For example, spatial precipitation downscaling enables the modeling of complex precipitation patterns using NNs. An additional benefit of NNs is a considerable reduction in computation time and energy [22]. First approaches for spatial precipitation downscaling with NNs [27] used a super resolution convolutional neural network (SRCNN, [9]). Convolutional neural networks (CNN) have shown their potential in downscaling low-resolution climate model outputs while outperforming other statistical approaches [2, 21, 28].

Traditional SR techniques first map the Low Resolution (LR) image to higher resolution (HR) usually with bi-cubic interpolation and subsequently learn the SR model in the higher dimensional space. This results in much higher computational requirements and [26] alternatively proposes to perform feature extraction in the LR space with the Efficient sub-pixel convolutional neural network (ESPCN).

Deep learning (DL) techniques have been used to predict floods with satisfactory results. CNN have proven to be promising due to their ability to process raw data in image format and reduce the number of parameters by using partially connected layers and weight sharing. [16] used deep CNNs trained from the outputs of 2D hydrodynamic model to predict the inundation depth caused by river flooding. [20] applied a U-Net based DL to model maximum water depths in an urban catchment using spatial inputs and rainfall characteristics.

In comparison to classical CNN approaches, generative adversarial networks (GANs) do not rely on a pre-defined expert metric, but instead utilize an evolving metric in the form of an individually trained neural network, [11]. GANs consist of two networks: a generator and a discriminator. The generator, typically a CNN, generates high-resolution images, whereas the discriminator evaluates the quality of the generated images by distinguishing between real and artificial images. The generator's task of trying to trick the discriminator is defined by the model's objective function [18, 31]. Both networks are simultaneously trained in an adversarial manner. This approach significantly increases the capacity to create more realistic results [30] and has been an effective method for generating high-resolution outputs [6]. In climate science, GANs can learn to reconstruct high-resolution solutions from climate model outputs and random components. [19] demonstrated the performance and capability of GANs within a spatial super-resolution approach by downscaling coarsened precipitation data with a 16 upscaling ratio. The same idea has also been applied to downscaling global precipitation forecasts [23].

The super-resolution methods based on GAN framework [18, 31] creates SR images that a discriminator cannot distinguish as a real HR image or an artificially super-resolved output. In this manner, HR images with better perceptual quality are generated. SRGAN [18] proposed to use an adversarial objective function. The main highlight of their work is a multi-task loss formulation that consists of three main parts: (1) a Mean Squared Error (MSE) loss that encodes pixel-wise similarity, (2) a perceptual similarity metric in terms of a distance metric defined over high-level image representation, and (3) an adversarial loss that balances a min-max game between a generator and a discriminator. The proposed framework basically favors outputs that are perceptually similar to the high-dimensional images. Since other techniques generally learn to optimize direct data dependent measures (such as pixel errors), [18] outperformed its competitors by a significant margin on the perceptual quality metric.

Recently, [15] applied a conditional generative adversarial network (cGAN), which is also CNN based, for predicting floods (floodGAN). Their approach uses spatially distributed rainfall as inputs to generate flood maps up to 10^6 times faster than physically based hydrodynamic modeling. However, the transferability

of their method to other locations is a major challenge because floodGAN is domain-specific due to the lack of topographic information used as inputs. Furthermore, cGANs have been used for generalized flood prediction in catchments not included in the training dataset [8], demonstrating the potential of GANs to adapt to unseen urban catchments and enhancing the scope of predictive models.

In this work, a downscaling framework is proposed that relies on super-resolution models to estimate High Resolution (HR) hydrodynamic variables from Low Resolution (LR) ones derived from upscaled flow simulations. The aim is to obtain fast and accurate estimates of HR flow fields for a given flooding configuration (building geometry) for any flow scenarios (initial and boundary conditions). The focus is on two indicators: the water depth and the norm of the unit discharge. One super-resolution model inspired from the ones developed in climate change studies and floods prediction are put forward. The first model is the Efficient sub-pixel convolutional neural network (ESPCN) in which the HR field is reconstructed with a periodic shuffling operator and MSE loss is used to calculate the difference between SR and HR variables. The model is compared to high resolution data over two synthetic configurations on a flat and variable topography. We evaluate the accuracy of super-resolution models to reconstruct HR fields in a steady-state and dynamic case. Their ability to enforce mass conservation and to generalize to unseen flood scenarios are also analyzed.

1 Models

1.1 Flow model and hazard indicators

In what follows, the reference HR model is the two-dimensional shallow water model, written in conservation form as

$$\partial_t u + \nabla \cdot F = S, \quad u = \begin{pmatrix} h \\ q \\ r \end{pmatrix}, \tag{1}$$

$$F = \begin{pmatrix} q & r \\ \frac{q^2}{h} + \frac{g}{2}h^2 & \frac{qr}{h} \\ \frac{qr}{h} & \frac{q^2}{h} + \frac{g}{2}h^2 \end{pmatrix}, \quad S = \begin{pmatrix} 0 \\ gh(S_{0,x} - S_{f,x} \\ gh(S_{0,y} - S_{f,y} \end{pmatrix} \tag{2}$$

$$\begin{pmatrix} S_{f,x} \\ S_{f,y} \end{pmatrix} = \frac{n^2}{h^{10/3}}|q|q \tag{3}$$

where g is the gravitational acceleration, h is the water depth, n is Manning's friction coefficient, $q = (q, r)$ is the unit discharge vector, $(S_{0,x}, S_{0,y})^T$ and $(S_{f,x}, S_{f,y})^T$ are respectively the bottom and friction slope vectors. The water depth h and the norm of the unit discharge $|q| = \sqrt{q^2 + r^2}$ are widely recognized as meaningful indicators for flood hazard. For the sake of conciseness, the analysis reported hereafter focuses on the water depth and the norm of the unit discharge vector, that are the most widely acknowledged indicators for flood hazard and the easiest variables to measure or compute.

1.2 Downscaling super-resolution framework

The proposed downscaling framework relies on image super-resolution (SR) approach which originates from computer vision. The task of SR is to estimate a HR image I^{SR} given a LR image I^{LR}. We will refer to r as the upscaling ratio between low and high resolutions. Both I^{LR} and I^{HR} are represented as real-valued tensors of size $H \times W$ and $rH \times rW$, respectively. Instead of recovering the LR image I^{LR} from the HR image I^{HR}, the LR image is obtained by solving the system (1) on a coarser mesh than the one used to generate the HR image. In this work, we use the super-resolution model introduced in [26] called Efficient Sub-Pixel CNN (ESPCN). In this architecture, we first apply l layer convolution neural network directly to

the LR image and then apply a sub-pixel deconvolution layer that upscales the LR feature maps to produce the super-resolution I^{SR}. For a network composed of L layers, the first $L-1$ layers can be described as follows:

$$f^1(I^{LR}; W_1, b_1) = \phi(W_1 * I^{LR} + b_1) \tag{4}$$

$$f^l(I^{LR}; W_{1:l}, b_{1:l}) = \phi(W_l * f^{l-1}(I^{LR}) + b_l) \tag{5}$$

where $W_l, b_l, l = 1, \cdots, L-1$ are learnable network weights and biases respectively. W_l is a 2D convolution tensor of size $n_{l-1} \times n_l \times k_l \times k_l$, where n_l is the number of features at layer l, $n_0 = 1$ and k_l is the filter size at layer l. The biases b_l are vectors of length n_l. The activation function ϕ is applied element-wise and is fixed. The last layer f^L has to convert the LR feature maps to a HR image I^{SR}. We pursue the following strategy to implement this operation:

$$I^{SR} = f^L(I^{LR}) = PS(W_L * f^{L-1}(I^{LR}) + b_L), \tag{6}$$

where PS is a periodic shuffling operator that rearranges the elements of a $H \times W \times r^2$ tensor to a tensor of shape $rH \times rW$. This operation writes

$$PS(T)_{x,y} = T_{\lfloor x/r \rfloor, \lfloor y/r \rfloor, r \mod (y,r) + \mod (x,r)}. \tag{7}$$

The Mean Squared Error (MSE) is used to calculate the difference between the super-resolution I^{SR} image generated by the network and the actual high resolution image. The loss function in ESPCN is given by:

$$MSE = \frac{1}{r^2 HW} \sum_{i=0}^{rH} \sum_{j=0}^{rW} \left(I^{HR}_{i,j} - f^L_{i,j}(I^{LR}) \right)^2 \tag{8}$$

2 Numerical experiments

To set up the statistical downscaling models for each considered flooding configuration, pairs of LR and HR flow simulations must be available from which LR and HR hazard indicators are derived. Within a given flooding configuration, the numerical values of the initial/boundary conditions are allowed to vary from one pair of simulations to the next, resulting in as many so-called flow scenarios. To ensure good performance of the statistical downscaling models, a number of flow scenarios must be available representing sufficiently consistent space-time behaviours of the flow fields. It is expected that, for a given configuration, once the downscaling models have seen a representative number of flow scenarios, they can be applied to flow scenarios that were not necessarily seen before.

2.1 Low and high resolution simulated data sets

A flooding configuration is defined as a given building geometry for which several flow scenarios, implemented with initial and/or boundary conditions, are considered. The HR data sets are obtained by solving the two-dimensional shallow water equations (1)-(3). The LR data sets are also obtained by solving equations (1)-(3) on a coarser mesh. We denote Ω_i^{LR} the ith computational cell in the LR mesh and $|\Omega_i^{LR}|$ its area. The mesh cells Ω_i^{LR} form a partition of the overall computational domain Ω. The upscaling ratio between the LR and HR meshes is given by:

$$r = \frac{|\Omega_i^{LR}|}{|\Omega_i^{HR}|}, \tag{9}$$

where Ω_i^{HR} is the ith computational cell in the HR mesh $|\Omega_i^{HR}|$ its area. A synthetic urban configuration is considered (Figure 1). It relies on a common layout consisting of a periodic array of length L made of buildings, aligned along the x-direction. The computational domain is discretised into a high resolution mesh with $80cm \times 80cm$ square cells, for 3575 cells in total. We consider an upscaling ration $r = 5$ and obtain

a low resolution mesh with $4m \times 4m$ square cells, for 147 cells in total. We consider here two synthetic configurations: in the first one, the bottom is flat and in the second some holes of 50cm are distributed among the streets. The water is initially at rest in the domain, with an initial depth $h_0 = 10^{-2}$ and an initial unit discharge $q = 0$. We run the flood simulations for $600s$. We split the border of the domain $\partial\Omega$ into three parts:

$$\begin{array}{lcl} \partial\Omega_1 & = & \{x = 0, y \in [0, 4]\} \\ \partial\Omega_2 & = & \{x = 200, y \in [0, 4]\} \\ \partial\Omega_3 & = & \{y = 0, x \in [0, 200]\} \cup \{y = 4, x \in [0, 200]\} \end{array} \tag{10}$$

At the border $\partial\Omega_1$, we impose a time-dependent unit discharge that increases linearly from 0 to q_1 for $t \in]0s, 150s]$, from q_1 to q_2 for $t \in]150s, 300s]$ and then decreases linearly from q_2 to 0 for $t \in]300s, 600s]$. At the border $\partial\Omega_2$, we impose a time-dependent boundary condition on the Froude number $Fr = \frac{|u|}{\sqrt{gh}}$. The Froude number increases linearly from 0 to 0.5 for $t \in]0s, 150s]$ and then stays constant until the end of the simulation. At the border $\partial\Omega_3$, we impose wall boundary conditions on the unit discharge $q = 0$. This setting can yield after some time iterations to the propagation of a shock wave into the domain and to wave reflections at crossroads and walls. Wave reflection phenomena introduce completely different hydraulic behaviors and patterns and are challenging to capture with a coarse mesh.

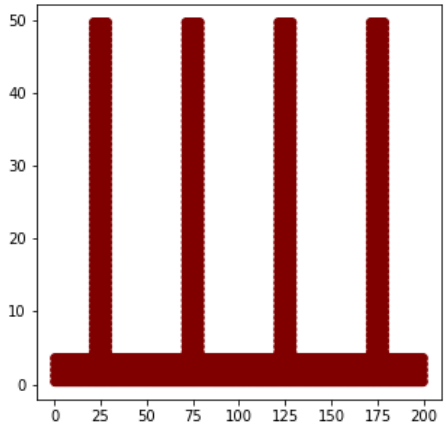

Figure 1: Synthetic urban configuration.

2.2 Training and test sets

Here, the focus is on the evaluation of model performance on previously unseen data to assess the so-called generalisation capability. The generalisation capability of a downscaling model may be measured in terms of performance, for a given configuration, at estimating flow scenarios that were not seen before. Thus, for each configuration, the training and test sets are defined as pairs of HR and LR hazard indicators simulated for a number of flow scenarios. The flow scenarios used to form the training and test sets are designed so as to span the space of boundary conditions. For our case study, fourteen flow scenarios are considered. The size of the training and tests depends on the length of the simulation time T and the sampling time step which are set as follows: $T = 600s$ and the sampling time step is 1s. Hence, each scenario generates 600 samples and they are distributed over the training and test sets as follows:

Let us note that the parameters (q_1, q_2) used in the training set spans the interval $[0.5, 1.5]^2$. In the test set, the two first scenarios depend on parameters belonging to $[0.5, 1.5]^2$ and the three others lie outside of this interval to evaluate the ability of the super-resolution models to generalize to unseen data.

Table 1: Flow scenarios defined in terms of boundary conditions (q_1, q_2) used to form the training and test sets for the two synthetic urban configurations (flat and variable topography).

Set	Boundary conditions (q_1, q_2)
Training	$(0.5, 0.5), (0.5, 1), (0.5, 1.5), (1, 0.5), (1, 1), (1, 1.5), (1.5, 0.5), (1.5, 1), (1.5, 1.5)$
Test	$(0.75, 1.25), (1.25, 0.75), (0.8, 2.1), (1.9, 0.95), (2, 2.5)$

2.3 Results and discussion

The performance of the ESPCN super-resolution model is evaluated on test sets made of 5 flow scenarios, different than the ones that constitute the training set, see Table 1. The performance evaluation on previously unseen data aims to estimate the generalisation capability of the super-resolution model. In Figure 2, the performance is provided in terms of the following relative error computed on the test sets for all configurations and for both hazard indicators h and $||q||$:

$$\frac{||X_{SR} - X_{HR}||}{||X_{HR}||}, \quad \frac{||X_{LR} - X_{HR}||}{||X_{HR}||}, \tag{11}$$

for $X = h$ or $X = ||q||$. The relative errors give the estimation error of the downscaling model relative to the error made when using LR hazard indicator as surrogates for HR hazard indicator values. The overall trend we observe in Figure 2 is the lack of accuracy of the the super-resolution model for the first time iterations of each test scenario. These snapshots correspond to the first seconds of the simulation where the discharge q is zero. The model fails to reconstruct this stationnary state even if the low resolution representation is correct. This issue is already observed on the training dataset and is not due to the ability of the model to generalize to unseen data. We are currently working on a specific data preprocessing that will improve the accuracy of the model for the reconstruction of steady states. Moreover, in the dynamic case, the relative error made by the super-resolution is way below the relative error of the LR hazard indicator. This statement is true for the two indicators, water depth and discharge norm, and in the case of flat or variable topography.

Table 2 provides, for each configuration and each test set, the minimum and maximal values taken by the water depth and discharge norm in the case of high, low and super-resolution. Following this indicator, the downscaling model performs well and manages to reconstruct the whole interval of water depth and discharge norm.

We seek now to compare the spatial profiles of the two hazard indicators in order to qualitatively assess their interpretability in terms of hydraulic behavior. To this end, we plot in Figure 3 the profiles of the water depth and discharge norm at the bottom of the domain 1. This part represents the main street of the urban configuration and each crossroad will display strong nonlinearities which are challenging to represent with a low resolution mesh. The downscaling model is capable of estimating complex spatial patters such as the ones simulated by refined shallow water models, starting from a lower quality representation of the flow fields. In the operational phase, this downscaling framework offers a considerable speedup over running a HR simulation for each new flow scenario. For instance, for one flow scenario 15 CPU s are needed to run the HR model. In comparison, running a LR simulation and downscaling the results using the ESPCN model requires 0.5 s. The speedup factor is thus 30.

3 Conclusion

The analyses carried out in this work showed that the proposed downscaling framework inspired from super-resolution may yield fast and accurate estimates of the HR hazard indicators. Further work is needed to understand how to bring improvements to this super-resolution model for a large number of flow scenarios. There is a need to investigate other model architectures than CNNs in order to improve the performance

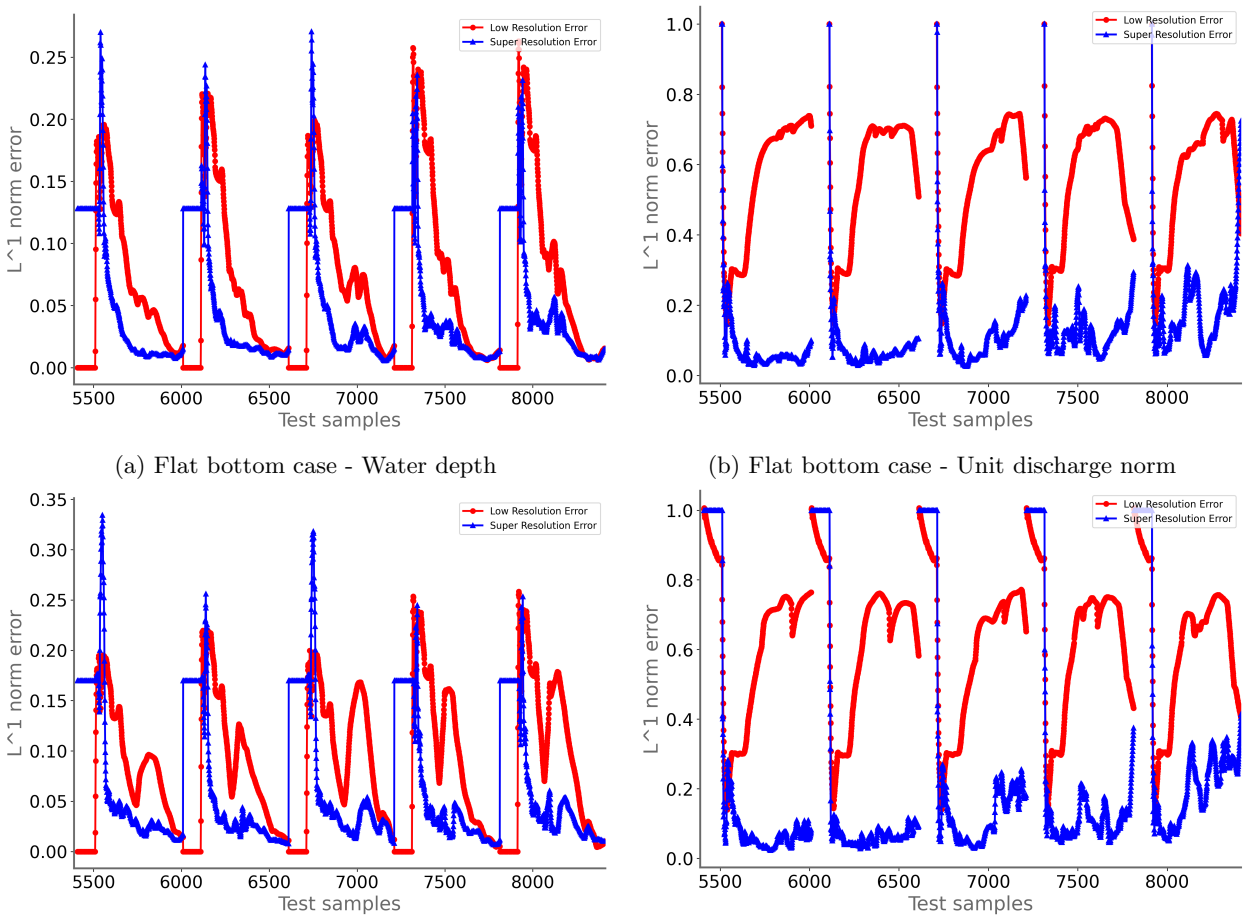

(a) Flat bottom case - Water depth

(b) Flat bottom case - Unit discharge norm

(c) Streets with holes - Water depth

(d) Streets with holes - Unit discharge norm

Figure 2: Error comparison between Low and Super Resolution for flat and variable topography test cases.

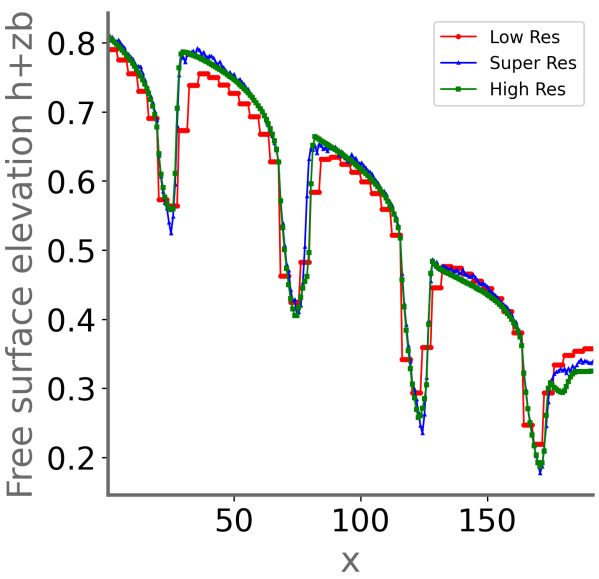

(a) Flat bottom case - Water depth

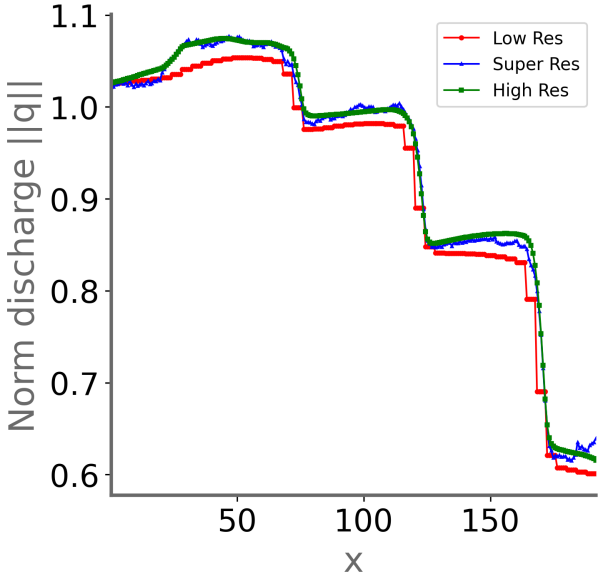

(b) Flat bottom case - Unit discharge norm

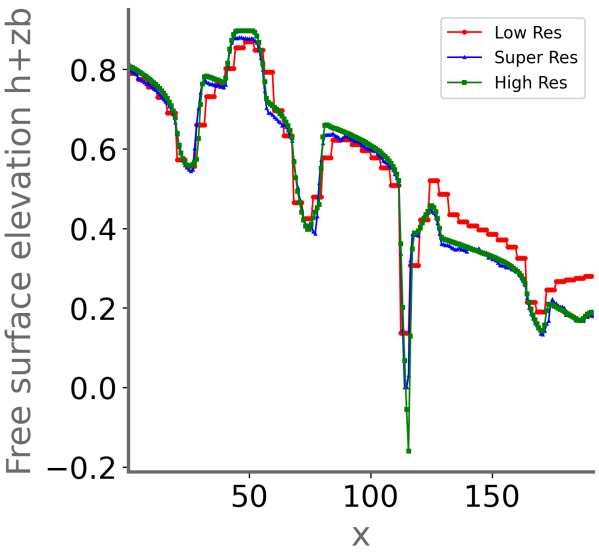

(c) Streets with holes - Water depth

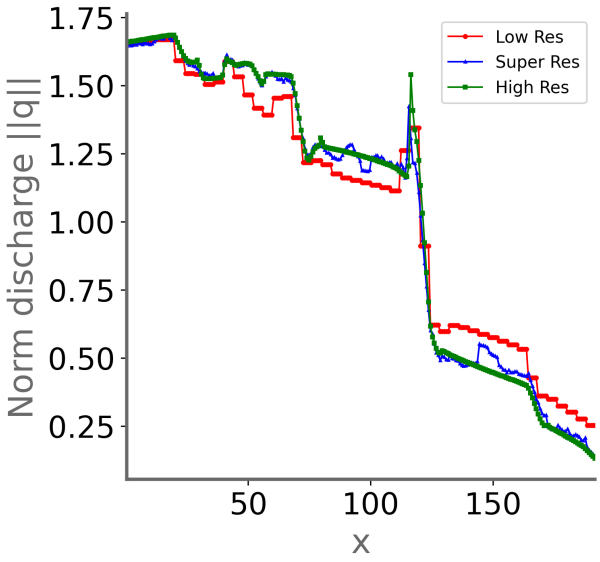

(d) Streets with holes - Unit discharge norm

Figure 3: Spatial profiles for flat and variable topography test cases.

Topography	Boundary conditions	$(\min h, \max h)$	$(\min \|\|q\|\|, \max \|\|q\|\|)$
Flat	Scenario $(q_1, q_2) \in [q_1^{\min}, q_1^{\max}] \times [q_2^{\min}, q_2^{\max}]$		
	LR	$(0, 0.661)$	$(0, 1.238)$
	HR	$(0, 0.672)$	$(0, 1.247)$
	SR	$(0, 0.676)$	$(0, 1.242)$
Flat	Scenario $(q_1, q_2) \notin [q_1^{\min}, q_1^{\max}] \times [q_2^{\min}, q_2^{\max}]$		
	LR	$(0, 1.005)$	$(0, 2.487)$
	HR	$(0, 1.042)$	$(0, 2.497)$
	SR	$(0, 1.047)$	$(0, 2.489)$
Variable	Scenario $(q_1, q_2) \in [q_1^{\min}, q_1^{\max}] \times [q_2^{\min}, q_2^{\max}]$		
	LR	$(0, 0.706)$	$(0, 1.13)$
	HR	$(-0.03, 0.722)$	$(-0.17, 1.14)$
	SR	$(0, 0.712)$	$(0, 1.13)$
Variable	Scenario $(q_1, q_2) \notin [q_1^{\min}, q_1^{\max}] \times [q_2^{\min}, q_2^{\max}]$		
	LR	$(0, 1.238)$	$(0, 2.487)$
	HR	$(0, 1.247)$	$(0, 2.497)$
	SR	$(0, 1.245)$	$(0, 2.527)$

Table 2: Minimum and maximum value of the HR, LR, SR free surface elevation and unit discharge norm for flat and variable topography test cases

of the downscaling strategy. One perspective for this work is to enrich the super-resolution models with the fundamental properties of the physical model like mass conservation, steady-states preservation and positivity of physical variables.

References

[1] Saeed Anwar, Salman Khan, and Nick Barnes. A deep journey into super-resolution: A survey. *ACM Comput. Surv.*, 53(3), May 2020.

[2] J. Baño-Medina, R. Manzanas, and J. M. Gutiérrez. Configuration and intercomparison of deep learning neural models for statistical downscaling. *Geoscientific Model Development*, 13(4):2109–2124, 2020.

[3] Killian Bakong, Vincent Guinot, Antoine Rousseau, and Gwladys Toulemonde. Downscaling shallow water simulations using artificial neural networks and boosted trees. *Discrete and Continuous Dynamical Systems - S*, 16(2):220–239, 2023.

[4] P.D Bates and A.P.J De Roo. A simple raster-based model for flood inundation simulation. *Journal of Hydrology*, 236(1):54–77, 2000.

[5] J. Carreau and V. Guinot. A PCA spatial pattern based artificial neural network downscaling model for urban flood hazard assessment. *Advances in Water Resources*, 147:103821, January 2021.

[6] M. Cheng, Fangxin Fang, Christopher C. Pain, and Ionel M. Navon. Data-driven modelling of non-linear spatio-temporal fluid flows using a deep convolutional generative adversarial network. *ArXiv*, abs/2004.00707, 2020.

[7] Jacinthe Clavet-Gaumont, David Huard, Anne Frigon, Kristina Koenig, Phillip Slota, Alain Rousseau, Iris Klein, Nathalie Thiémonge, Fanny Houdré, John Perdikaris, Richard Turcotte, Julie Lafleur, and Bruno Larouche. Probable maximum flood in a changing climate: An overview for Canadian basins. *Journal of Hydrology: Regional Studies*, 13:11–25, 2017.

[8] Cesar A.F. Do Lago, Marcio H. Giacomoni, Roberto Bentivoglio, Riccardo Taormina, Marcus N. Gomes, and Eduardo M. Mendiondo. Generalizing rapid flood predictions to unseen urban catchments with conditional generative adversarial networks. *Journal of Hydrology*, 618:129276, March 2023.

[9] Chao Dong, Chen Change Loy, Kaiming He, and Xiaoou Tang. Learning a deep convolutional network for image super-resolution. In *European Conference on Computer Vision*, 2014.

[10] Alessia Ferrari, Daniele P. Viero, Renato Vacondio, Andrea Defina, and Paolo Mignosa. Flood inundation modeling in urbanized areas: A mesh-independent porosity approach with anisotropic friction. *Advances in Water Resources*, 125:98–113, 2019.

[11] Ian Goodfellow, Jean Pouget-Abadie, Mehdi Mirza, Bing Xu, David Warde-Farley, Sherjil Ozair, Aaron Courville, and Yoshua Bengio. Generative adversarial networks. *Commun. ACM*, 63(11):139–144, October 2020.

[12] Vincent Guinot. Multiple porosity shallow water models for macroscopic modelling of urban floods. *Advances in Water Resources*, 37:40–72, 2012.

[13] Vincent Guinot, Brett F. Sanders, and Jochen E. Schubert. Dual integral porosity shallow water model for urban flood modelling. *Advances in Water Resources*, 103:16–31, 2017.

[14] Vincent Guinot and Sandra Soares-Frazão. Flux and source term discretization in two-dimensional shallow water models with porosity on unstructured grids. *International Journal for Numerical Methods in Fluids*, 50(3):309–345, 2006.

[15] Julian Hofmann and Holger Schüttrumpf. floodGAN: Using Deep Adversarial Learning to Predict Pluvial Flooding in Real Time. *Water*, 13(16):2255, August 2021.

[16] Syed Kabir, Sandhya Patidar, Xilin Xia, Qiuhua Liang, Jeffrey Neal, and Gareth Pender. A deep convolutional neural network model for rapid prediction of fluvial flood inundation. *Journal of Hydrology*, 590:125481, 2020.

[17] Byunghyun Kim, Brett F. Sanders, James S. Famiglietti, and Vincent Guinot. Urban flood modeling with porous shallow-water equations: A case study of model errors in the presence of anisotropic porosity. *Journal of Hydrology*, 523:680–692, 2015.

[18] Christian Ledig, Lucas Theis, Ferenc Huszár, Jose Caballero, Andrew Cunningham, Alejandro Acosta, Andrew Aitken, Alykhan Tejani, Johannes Totz, Zehan Wang, and Wenzhe Shi. Photo-realistic single image super-resolution using a generative adversarial network. In *2017 IEEE Conference on Computer Vision and Pattern Recognition (CVPR)*, pages 105–114, 2017.

[19] Jussi Leinonen, Daniele Nerini, and Alexis Berne. Stochastic super-resolution for downscaling time-evolving atmospheric fields with a generative adversarial network. *IEEE Transactions on Geoscience and Remote Sensing*, 59(9):7211–7223, 2021.

[20] Roland Löwe, Julian Böhm, David Getreuer Jensen, Jorge Leandro, and Søren Højmark Rasmussen. U-flood – topographic deep learning for predicting urban pluvial flood water depth. *Journal of Hydrology*, 603, 2021.

[21] Bin Mu, Bo Qin, Shijin Yuan, and Xiaoyun Qin. A climate downscaling deep learning model considering the multiscale spatial correlations and chaos of meteorological events. *Mathematical Problems in Engineering*, 2020(1):7897824, 2020.

[22] Jaideep Pathak, Shashank Subramanian, Peter Z. Harrington, Sanjeev Raja, Ashesh Chattopadhyay, Morteza Mardani, Thorsten Kurth, David Hall, Zong-Yi Li, Kamyar Azizzadenesheli, Pedram Hassanzadeh, Karthik Kashinath, and Anima Anandkumar. Fourcastnet: A global data-driven high-resolution weather model using adaptive fourier neural operators. *ArXiv*, abs/2202.11214, 2022.

[23] Ilan Price and Stephan Rasp. Increasing the accuracy and resolution of precipitation forecasts using deep generative models. *ArXiv*, abs/2203.12297, 2022.

[24] Brett F. Sanders and Jochen E. Schubert. PRIMo: Parallel raster inundation model. *Advances in Water Resources*, 126:79–95, 2019.

[25] Brett F. Sanders, Jochen E. Schubert, and Humberto A. Gallegos. Integral formulation of shallow-water equations with anisotropic porosity for urban flood modeling. *Journal of Hydrology*, 362(1):19–38, 2008.

[26] Wenzhe Shi, Jose Caballero, Ferenc Huszár, Johannes Totz, Andrew P. Aitken, Rob Bishop, Daniel Rueckert, and Zehan Wang. Real-Time Single Image and Video Super-Resolution Using an Efficient Sub-Pixel Convolutional Neural Network, September 2016.

[27] Thomas Vandal, Evan Kodra, Sangram Ganguly, Andrew Michaelis, Ramakrishna Nemani, and Auroop R. Ganguly. Deepsd: Generating high resolution climate change projections through single image super-resolution. In *Proceedings of the 23rd ACM SIGKDD International Conference on Knowledge Discovery and Data Mining*, KDD '17, page 1663–1672, New York, NY, USA, 2017. Association for Computing Machinery.

[28] A. Vaughan, W. Tebbutt, J. S. Hosking, and R. E. Turner. Convolutional conditional neural processes for local climate downscaling. *Geoscientific Model Development*, 15(1):251–268, 2022.

[29] Daniele P. Viero. Modelling urban floods using a finite element staggered scheme with an anisotropic dual porosity model. *Journal of Hydrology*, 568:247–259, 2019.

[30] Kunfeng Wang, Chao Gou, Yanjie Duan, Yilun Lin, Xinhu Zheng, and Fei yue Wang. Generative adversarial networks: introduction and outlook. *IEEE/CAA Journal of Automatica Sinica*, 4:588–598, 2017.

[31] Xintao Wang, Ke Yu, Shixiang Wu, Jinjin Gu, Yihao Liu, Chao Dong, Yu Qiao, and Chen Change Loy. Esrgan: Enhanced super-resolution generative adversarial networks. In Laura Leal-Taixé and Stefan Roth, editors, *Computer Vision – ECCV 2018 Workshops*, pages 63–79, Cham, 2019. Springer International Publishing.

[32] Ilhan Özgen, Jiaheng Zhao, Dongfang Liang, and Reinhard Hinkelmann. Urban flood modeling using shallow water equations with depth-dependent anisotropic porosity. *Journal of Hydrology*, 541:1165–1184, 2016.